Earth and Planetary Science Letters 477 (2017) 1–13

Contents lists available at ScienceDirect

Earth and Planetary Science Letters

www.elsevier.com/locate/epsl

Pervasive seismic low-velocity zones within stagnant plates in the mantle transition zone: Thermal or compositional origin?

B. Tauzin [a,b], S. Kim [c,*], B.L.N. Kennett [b]

[a] Laboratoire de Géologie de Lyon: Terre, Planètes, Environnement, Université de Lyon, Université Lyon 1 and Ecole Normale Supérieure de Lyon, UMR CNRS 5276, F-69622 Villeurbanne, France
[b] Research School of Earth Sciences, Australian National University, Canberra, Australian Capital Territory 0200, Australia
[c] School of Earth and Environmental Sciences, Seoul National University, Seoul, 08826, Republic of Korea

ARTICLE INFO

Article history:
Received 1 May 2017
Received in revised form 2 August 2017
Accepted 3 August 2017
Available online xxxx
Editor: P. Shearer

Keywords:
mantle transition zone
northeast Asia margin
northwest Pacific
receiver functions
low-velocity zones

ABSTRACT

We exploit conversions between P and S waves for large-scale, high-resolution imaging of the mantle transition zone beneath Northwest Pacific and the margin of Eastern Asia. We find pervasive reflectivity concentrated in two bands with apparent wave-speed reduction of −2% to −4% about 50 km thick at the top of the transition zone and 100 km thick at the bottom. This negative reflectivity associated with the scattered-waves at depth is interpreted jointly with larger-scale mantle tomographic images, and is shown to delineate the stagnant portions of the subducted Pacific plate in the transition zone, with largely positive shear-wave velocity contrasts. The upper reflectivity zone connects to broad low-velocity regions below major intra-plate volcanoes, whereas the lower zone coincides locally with the occurrence of deep-focus earthquakes along the East Asia margin. Similar reflectivity is found in Pacific Northwest of the USA. We demonstrate that the thermal signature of plates alone is not sufficient to explain such features. Alternative explanations for these reflective zones include kinetic effects on olivine phase transitions (meta-stability), compositional heterogeneities within and above stagnant plates, complex wave-propagation effects in the heterogeneous slab structure, or a combination of such factors. We speculate that part of the negative reflectivity is the signature of compositional heterogeneities, as revealed by numerous other studies of seismic scattering throughout the mantle, and that such features could be widespread across the globe.

1. Introduction

The 250 km-thick boundary layer of the mantle transition zone (MTZ) is delimited by two seismic interfaces, the '410' and '660'-km discontinuities, and separates the upper mantle from the more viscous lower mantle. The seismic discontinuities at the top and bottom of the MTZ are commonly attributed to solid–solid mineralogical phase changes from olivine (*ol*) to wadsleyite (*wa*) at 410 km depth, and ringwodite (rw) to perovskite+magnesiowustite ($pv + mw$) at 660 km depth (e.g. Bina and Helffrich, 1994).

There are many observations of scattering of seismic waves near or within the MTZ. In the shallow to mid-lower mantle, seismic array studies have located many small-scale scatterers in association with subducted plates in the circum Pacific region (e.g. Niu, 2014; see Kaneshima, 2016 for a review). Within the MTZ, Bentham and Rost (2014) showed from P-P scattering that a good correlation exists between the location of scatterers and the edges of high seismic wave speeds in tomographic models, delineating subducted plates below Western Pacific. These scatterers have dominantly a low-velocity signature (Kaneshima, 2016). Such scattering is usually attributed to the presence of small-scale and compositionally distinct remnants of subducted oceanic crust. The mid-oceanic ridge basalts (MORB), in large proportion in the oceanic crust, have indeed a different seismic signature than the harzburgite (the underlying depleted mantle layer in subducted oceanic plates), or pyrolite (the parental mantle) in various pressure ranges (e.g. Ricard et al., 2005; Stixrude and Lithgow-Bertelloni, 2005).

Larger-scale coherent zones of scattering exist also with dispersed geographical and depth distributions within and surrounding the MTZ. These zones have mainly been reported from P-to-S receiver function studies and described as low shear-wave velocity (*vs*) layers. The estimated shear-wave velocity contrast, Δvs, at the top of these layers ranges from −2 to −8%. An early observation came from a multiple-ScS reverberation study by Revenaugh and Sipkin (1994), who imaged a ∼5.8% impedance decrease be-

* Corresponding author.
E-mail address: srk@snu.ac.kr (S. Kim).

http://dx.doi.org/10.1016/j.epsl.2017.08.006

neath the Sea of Japan (East Sea), Yellow Sea and easternmost Asia at around 330 km depth on top of the *ol* → *wa* transition. Subsequently, other studies from receiver functions, P-wave triplications, and ScS reverberations, reported many apparent low-velocity zones (LVZs) with thicknesses varying from 20 to 90 km on top of the 410-km discontinuity. These zones were found in various geodynamical settings: the subduction zones in the western US and southwest Pacific (Song et al., 2004; Courtier and Revenaugh, 2007; Tauzin et al., 2013); regions of hot upwelling in the vicinity of ancient continental platforms (Vinnik and Farra, 2007); or globally, in regions with no particular affinity with a specific geodynamical context (Tauzin et al., 2010).

Apparent low shear-wave velocity layers have also been found atop the *rw* → *pv*+*mw* phase change. Shen and Blum (2003) found a layer in an area of ancient slab subduction in southern Africa. In the western US, the top of these zones appears near 590 km depth in close association with the subducted Farallon plate (Tauzin et al., 2013). In northeastern China and probably extending beneath the Eurasian continent, Shen et al. (2008), Gao et al. (2010) and Liu et al. (2015) reported from receiver functions a zone of negative reflectivity within or near the stagnant Pacific plate. Similar seismic signatures have been reported for subduction zones in Europe although these may result in part from imaging artifacts, due in particular to seismic wave reverberations in the shallow upper mantle (Cottaar and Deuss, 2016).

Negative reflectivity zones atop and at the bottom of the MTZ are usually reported and discussed separately so there is currently no common ground for interpretation. They have often been attributed to different mechanisms involving variations in mantle major and minor element chemistry. In this way, the negative reflectivity detected above the *ol* → *wa* transition is often interpreted as arising from partial melting, induced by the dehydration of mantle rocks (Revenaugh and Sipkin, 1994; Bercovici and Karato, 2003; Song et al., 2004; Vinnik and Farra, 2007; Tauzin et al., 2010). The reflective zone atop the *rw* → *pv* + *mw* phase change is enigmatic. It is often attributed to compositional stratification due to the accumulation of low-velocity oceanic crust through crustal decoupling from subducted plates (Ringwood and Irifune, 1988; Van Keken et al., 1996; Shen and Blum, 2003; Shen et al., 2014). Shen et al. (2014) suggest that these zones above the 660 could be global in nature, resulting from crustal accumulation during the 3 to 4.1 Gyr long history of plate subduction in the Earth's mantle.

Regionally in the coldest subduction zones, zones of anomalous reflectivity can arise from solid–solid phase transformations. When subducted oceanic plates penetrate into the deep mantle and reach the depth of the top of the transition zone, *ol* in the subducted plate transforms into the higher-pressure and higher-density form *wa*. Within the coldest core of the subducting plate, this transformation may be delayed due to kinetic effects, which would allow metastable olivine to persist deeper than 410 km depth. The *ol* having slower seismic signature than *wa*, the resulting seismic response is an apparent low-velocity zone. Several lines of evidence point toward the existence of a meta-stable olivine wedge (MOW) within the Pacific slab under northeast Asia (Iidaka and Suetsugu, 1992; Kawakatsu and Yoshioka, 2011). The wedges are reported down to 4500–570 km depth and with a −3 to −9% Δ*vs* contrast. Kawakatsu and Yoshioka (2011) presented from receiver function imaging with the Hi–Net network in southwest Japan an image of the MOW in the subducting Pacific plate as a thin (10–15 km) westward dipping low-velocity layer surrounded by sharp boundaries at depths between ∼350 km and 450 km.

Widespread Cenozoic to recent intraplate volcanism in northeast China and the Korean Peninsula, and deep focus earthquakes within the MTZ below the Japan Sea, may well be linked to the presence of deep compositional heterogeneities or a MOW

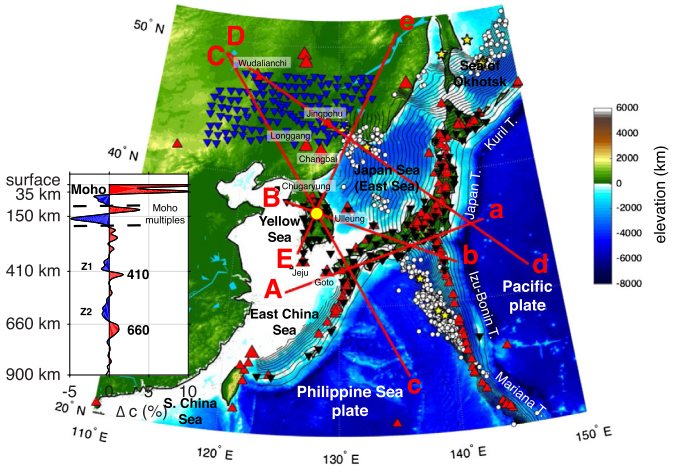

Fig. 1. Map of study region with the 232 stations used in our receiver function analysis, along with the lines for cross sections for the 2D images shown in Figs. 2–6. The subducted Pacific and Philippine plate depth contours are shown with black lines from 20 to 720 km depth. Small red triangles indicate arc-related volcanoes. Larger red triangles designate intra-plate volcanoes. White dots correspond to the location of deep focus subduction zone earthquakes within the transition zone from the U.S. Geological Survey (USGS), the yellow stars representing events with magnitude greater than 7.0. Seismic stations are shown with inverted triangles: in blue the NECESSArray, in black F-Net in Japan, and in black the permanent networks in Korea. Our 2D images are constructed from the juxtaposition of radial profiles such as shown in the inset for the location marked by the yellow dot in South Korea.

in the northwest Pacific subduction zones. The Changbai volcano (Fig. 1), located at the border between China and North Korea, is the largest and most active intraplate volcano in northeast Asia. Some authors have related this volcano as well as others (Wudalianchi, Jingpohu, Longgang, Chugaryung, Ulleung, Jeju and Goto; see Fig. 1) to hot and hydrated upwellings from the Pacific plate that is stagnant within the MTZ. This model proposes that the Pacific slab brings hydrous minerals down to MTZ depths, either as in-slab dense hydrous magnesium silicates (e.g. the phase A; e.g. Ohtani et al., 2001) or through entrainment of hydrated nominally anhydrous minerals above the slab (olivine, garnet, pyroxene). Convective instabilities may occur from the top of the stagnant plate, which is heated from above (Richard and Bercovici, 2009). Due to the lower water solubility in *ol* (Kohlstedt et al., 1996), these upwelling plumes in the *wa* stability field may release their water and induce partial melting when transforming to *ol* atop the 410-km discontinuity (Bercovici and Karato, 2003; Richard and Bercovici, 2009). This water-rich upwelling might further ascend through the asthenosphere and lithosphere, and lead to intraplate volcanism through fluid-assisted decompression melting (e.g., Richard and Iwamori, 2010; Kim et al., 2016). In these circumstances, variations in MTZ hydration could support the occurrence of vigorous small-scale convection in the mantle below northeast China, and a hydrous partial melt layer atop the 410 (a LVZ) would be a key marker of this model.

Deep-focus earthquakes occur in the subducted Pacific plate east of the Changbai, Jingpohu and Ulleung intraplate volcanoes at depths beyond 550 km (Fig. 1). The physical mechanism that triggers and sustains earthquake ruptures at such depths remains controversial (Green and Houston, 1995; Kawakatsu and Yoshioka, 2011). Mechanisms include transformational faulting triggered by metastable *ol* transforming to *wa* in the cold core of the slab, thermal instability and runaway shear melting when the deformation of material occurs rapidly enough in comparison with the time scale of thermal diffusion, grain size assisted thermal runaway, dehydration embrittlement upon exsolution of a volatile component

like water, or partial melting of carbonates that provides a fault-lubricating fluid (e.g. Ye et al., 2016). The properties of the material surrounding the source region of deep subduction zone earthquakes (e.g. highly fractured material, melting, phase changes) may also determine the mechanism of dissipation and the energy available for seismic radiation.

In this study we employ systematic two-dimensional (2D) receiver function imaging of the MTZ in the Northwestern Pacific and Eastern Asia regions, to show that a dipping low-velocity zone indeed exists in the MTZ below southwest Japan. Moreover, we find pervasive seismic reflectivity with a negative signature in many places in the region. This broad reflectivity concentrates in two bands on top of stagnant plates in the MTZ and at their base. Similar features exist in the MTZ below the northwestern US. The presence of such features over such large and disparate regions suggests that the apparent LVZs seen in receiver function imaging are not exclusively the result from delayed kinetics of MTZ phase transitions. We speculate that these zones are the result of compositional heterogeneities within or near the stagnant plates and discuss potential implications for deep subduction zone seismicity and intraplate volcanism for the East Asia margin.

2. Receiver function imaging

We refer to the supplementary material for details of the methodology used to image the mantle and transition zone structure from receiver functions (RFs) (Section S1). We use the waveforms of 531 teleseismic earthquakes recorded at 232 three-component broad-band seismic stations (Fig. 1) located on the Korean peninsula, in Japan (F-Net), and from a temporary array in northeast China (NECESSArray). We use iterative time-domain deconvolution (Ligorría and Ammon, 1999). After selection based on signal-to noise ratio, the final RF dataset is composed of 41,814 waveforms and provides a good coverage of P-to-S piercing points across the 410 and 660-km discontinuities below the area (Fig. S1). Receiver functions are combined using a common conversion point (CCP) stacking approach. We refer to the work of Tauzin et al. (2013) and the supplementary material for the details of the method. We use the *iasp91* velocity model (Kennett and Engdahl, 1991) for ray-tracing and computation of travel-times. As discussed in Section 5, the use of a three-dimensional *vs* model from linearized tomographic inversion does not have much effect on the overall reflectivity patterns observed around and within the MTZ. Our imaging procedure includes a smoothing operation (see Section S1 in the supplementary material). In Fig. S2, we illustrate the effect of applying this operation on the A-a profile (Fig. 1). The seismic structure remains clearly identifiable. We also apply a bootstrap resampling approach (Efron and Tibshirani, 1990) to estimate the noise in seismic images (Figs. S13–S14).

In Fig. 1 we identify five profiles for which we present the result of CCP stacking of receiver function (RFs). The first profile, A-a (Fig. 2), is chosen in southwest Japan following up the results of Kawakatsu and Yoshioka (2011). We test their observation of a single low-velocity layer between 350 and 450 km depth associated with a MOW in the subducting Pacific plate. The other profiles across China, Korea and Japan (B-b in Fig. 3), Korea–Japan (C-c in Fig. 4), China-Japan (D-d in Fig. 5), and Korea–China (E-e in Fig. 6) are chosen to emphasize the correlation between reflectivity patterns from RF data, shear-wave velocity anomalies in global and regional mantle tomographic models, and deep earthquake hypocenters in the MTZ. Additional cross-sections for profiles across the NECESSArray portable experiment in China are also provided (Figs. S9–S10).

In the Supplementary Material (Figs. S4–S8), our CCP stacked cross-sections are compared with the result of modeling wave-

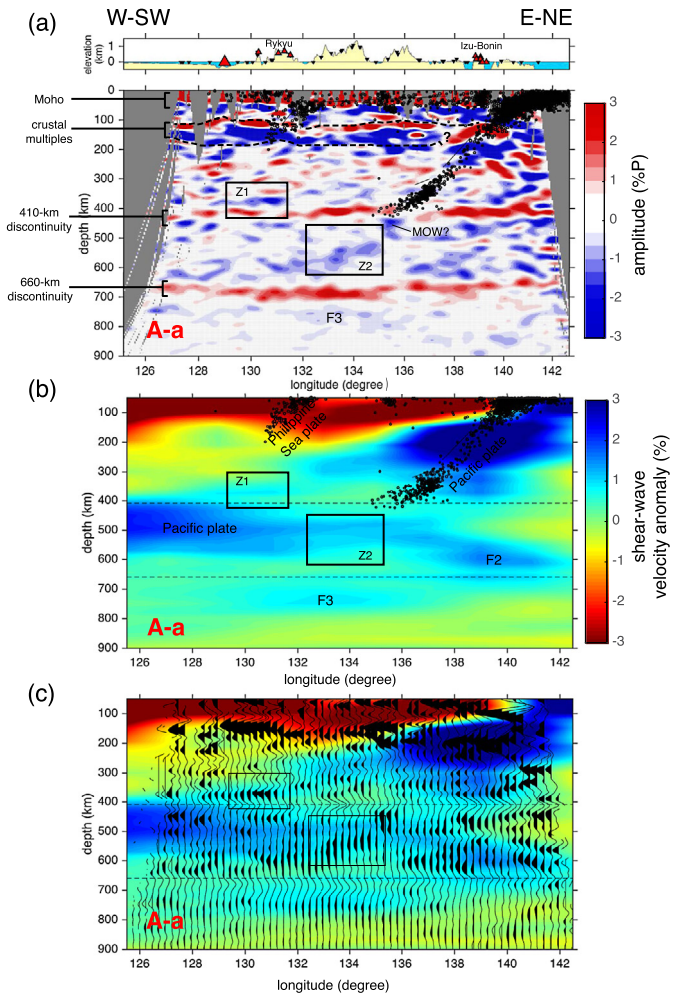

Fig. 2. (a) 2D CCP seismic section for the A-a profile across Japan. Positive/negative amplitudes are shown in red/blue and mark shear-wave velocity increases/decreases. This A-a profile is the same as used by Kawakatsu and Yoshioka (2011). The topography is plotted in the uppermost panel. The seismicity (black dots) is mainly due to the subduction of the Pacific plate below the Izu-Bonin/Japan trench and of the Philippine Sea plate at the Ryukyu trench. The slab geometry (Hayes et al., 2012) is plotted with thin black lines. The 410 and 660 discontinuities are labeled. The frames highlight regions of the MTZ discussed in the text. (b) Cross-section along the A-a profile through the shear-wave velocity model of Debayle and Ricard (2012). Based on the plate contour from Hayes et al. (2012), the high velocity anomaly inside the transition zone between longitudes 126–130°E is labeled as Pacific plate, but is associated in some models with the subduction of the Philippine Sea plate. (c) Superimposition of the CCP section on the tomographic model of Debayle and Ricard (2012) – negative amplitudes are emphasized in black.

propagation in the *iasp91* velocity structure. These synthetic tests show the influence of heterogeneous path coverage on seismic amplitudes, which is more significant at the base of the transition zone as the ray paths spread, but remains significantly smaller than the features observed in CCP stacks.

We compare our RF images with three global tomographic models and one regional model. For brevity, we display only here the comparison with the model from Debayle and Ricard (2012); the comparison with the other three models is made in the Supplementary Material (Figs. S11–S12).

In the seismic cross-sections (Figs. 2–6), positive amplitudes shown in red correspond to a downward increase of velocity ($\Delta vs > 0$) and negative amplitudes (blue) to a velocity reduction ($\Delta vs < 0$). The present seismic images are based on a ternary color code (red–white–blue), sufficiently simple to allow the reader to identify the correlation between CCP stacked signals and seis-

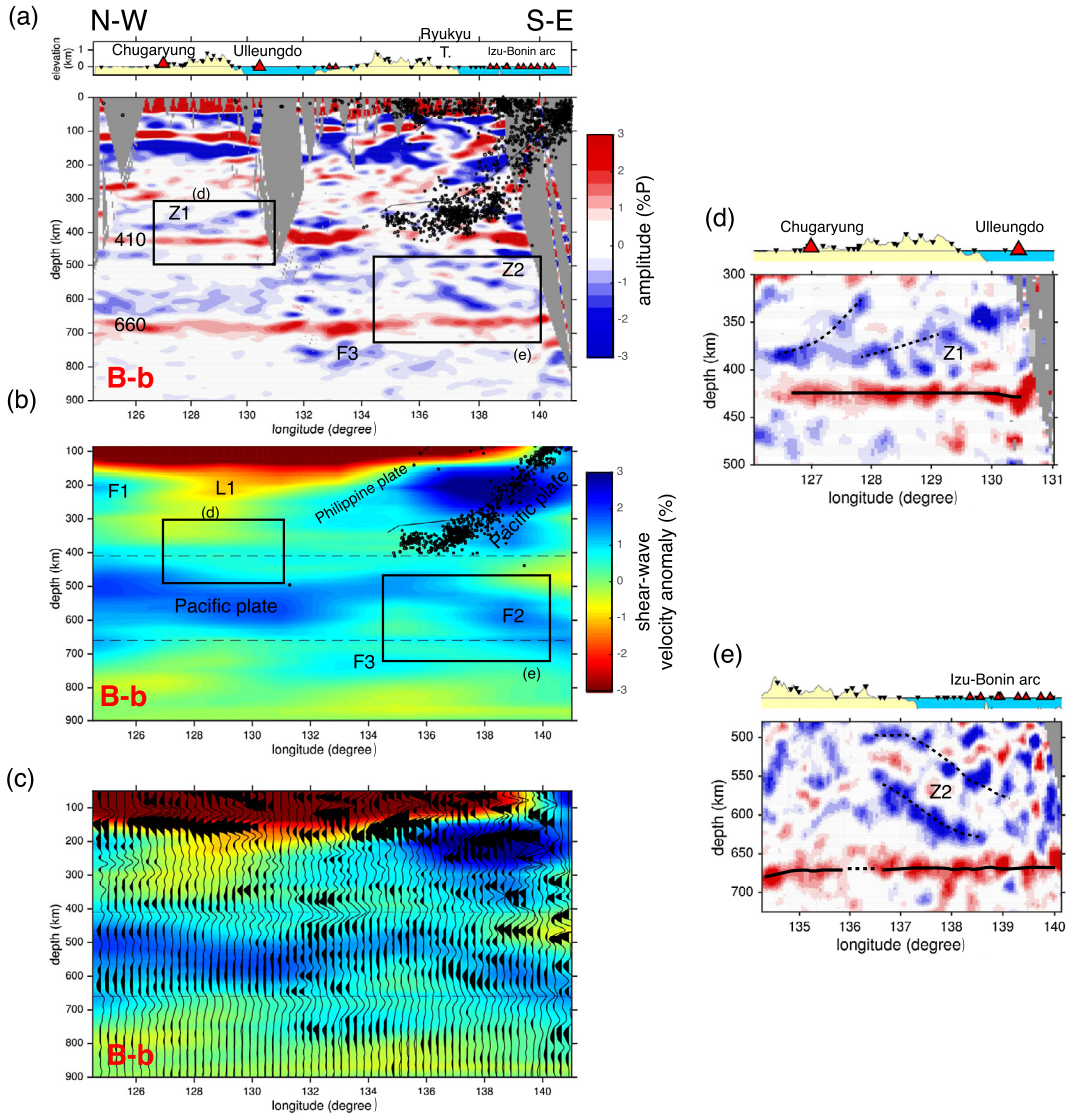

Fig. 3. (a) CCP section for the B-b profile across Korea and Japan. Positive/negative amplitudes are shown in red/blue and mark shear-wave velocity increase/decrease. The two insets correspond to enlargements of the results show in panels (d) and (e). The zone labeled MOW could be the metastable olivine wedge identified by Kawakatsu and Yoshioka (2011). (b) Cross-section along the B-b profile through the shear-wave velocity model of Debayle and Ricard (2012). Based on the plate contour from Hayes et al. (2012), the high velocity anomaly inside the transition zone between longitudes 126–130°E is labeled as Pacific plate, but is associated in some models with the subduction of the Philippine Sea plate. (c) Superimposition of the CCP section on the tomographic model – negative amplitudes are emphasized in black. (d) Enlarged view around the 410-km discontinuity in the region below the Chugaryung and Ulleungdo volcanoes in Korea. The Z1 negative signals tend to shallower toward the Ulleungdo volcano. (e) Enlarged view around the 660-km discontinuity. The Z2 zone of reflectivity has a distinctive pattern following the seismic signature of the stagnant plate in the MTZ.

mic tomography. In these images, most seismic signals are robust according to the confidence interval obtained from bootstrap resampling, as shown in the two examples in Fig. S13. We focus our discussion on certain features of the CCP stacks, but this does not mean that we ignore other features that seem to be just as well resolved. The negative features discussed here are pervasive within two depth intervals, and we therefore denote as Z1 and Z2 all the negative features within these two depth intervals.

We built maps of the geographical distribution of negative reflective zones in two distinct depth windows (see Figs. 7 and 8), following Tauzin et al. (2013) and as detailed in the supplementary material (Section S1). These depth windows are from 325 to 400 km depth for the shallower negative reflective zone Z1, and from 550 to 650 km depth for the deeper negative reflective zone Z2. The lateral variations of seismic amplitudes, within their uncertainties, provide an indication as to whether a negative zone is present or not (Figs. 7 and 8).

3. Results

3.1. Profiles across southwest Japan (A-a) and Korea–Japan (B-b)

In Fig. 2a, the CCP stacked signal along profile A-a through western Japan is plotted together with the intermediate-depth and deep seismicity (black dots) and the slab geometry (Hayes et al., 2012). This image clearly reveals the multiple reverberations in the crust of the main Japanese islands, seen as positive-over-negative signals between 100 and 200 km depth. The two downward increases of velocities at the 410 and 660-km discontinuities are very clear (as red bands). The overall topography of the boundaries of the MTZ is consistent with the observations from Kawakatsu and Yoshioka (2011): an uplift of the 410 at the intersection of the seismicity-delineated slab and a broad (~700 km) apparent deepening of the 660 between 129°W and 136°W.

Most other signals within or surrounding the MTZ have negative amplitudes (shown in blue). These features include: (i) a dip-

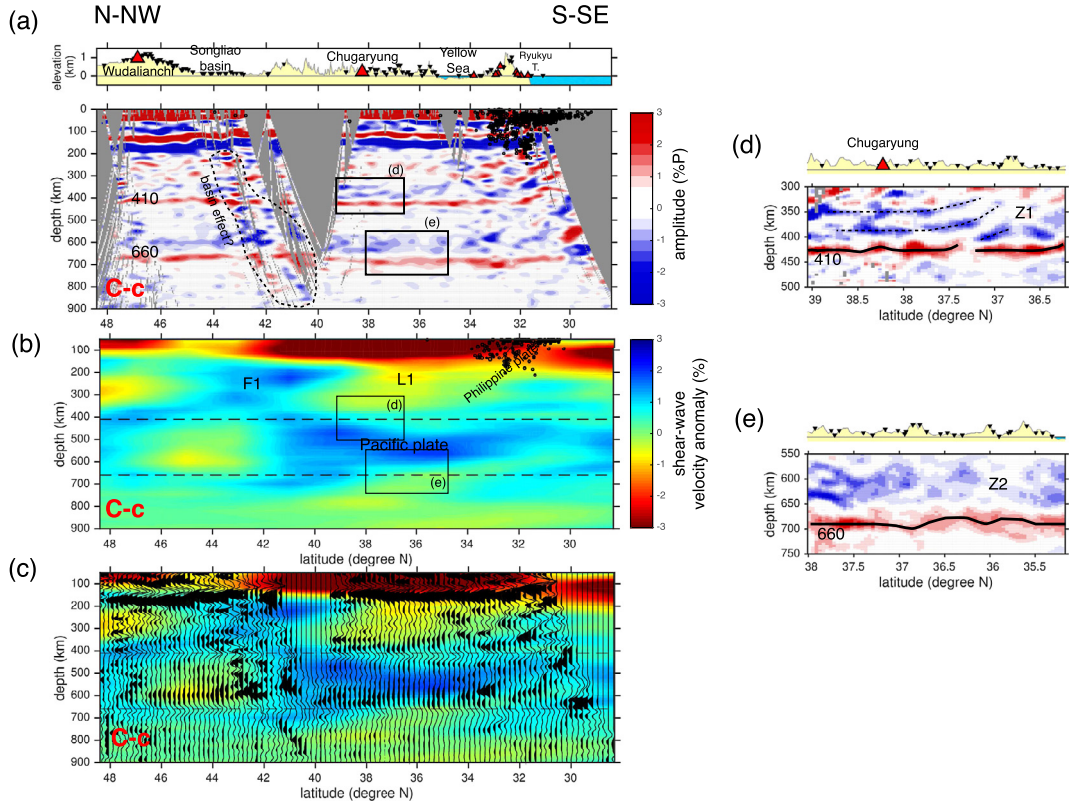

Fig. 4. (a) A 2D CCP seismic section for the C-c profile across China, Korea and Japan. Positive/negative amplitudes are shown in red/blue and mark shear-wave velocity increase/decrease. The topography is shown in the uppermost panel. The seismicity (black dots) is associated with the subduction of the Philippine plate at the Ryukyu trench. The 410 and 660 discontinuities are labeled. The region contoured with a black dashed line below the Songliao sedimentary basin is possibly blurred by strong reverberations. The two insets correspond to enlarged views of the results shown in panels (d) and (e). (b) Cross-section along the C-c profile through the shear-wave velocity model of Debayle and Ricard (2012). (c) Superimposition of the CCP section on the tomographic model of Debayle and Ricard (2012) – negative amplitudes are emphasized in black. (d) Enlarged view around the 410-km discontinuity in the region below the Chugaryung volcano at the border between South and North Korea. The 410 is delineated with a black line. Multiple negative signals are labeled Z1 and emphasized with dashed arrows. (e) Enlarged view around the 660-km discontinuity. A ∼100-km thick zone of negative amplitudes above the 660 is labeled Z2.

ping signal labeled Z2 in the prolongation of the slab seismicity from ∼450 km depth to the base of the transition zone (∼630 km depth), (ii) a flat negative signal atop the 410, labeled Z1. In the following, we describe Z2 as the deeper zone of reflectivity at the base of the MTZ, and Z1 as the shallower zone of reflectivity on top of the 410. Along profile A-a, it is clear that the extent of Z2 is not limited to the prolongation of the slab. Z2 flattens against the 660 west of 132°E and an isolated pattern of negative reflectivity appears also in the lowermost MTZ between 136°W and 140°W. Z2 and to a lesser extent Z1 are also discernable on the unsmoothed seismic images (Fig. S2), and reveal a significant small-scale granularity.

The amplitude of the negative Z1 and Z2 signals is approximately half the amplitude of the conversion at the 410-km discontinuity in the inset in Fig. 1 but can be as strong as the signal of the 410-km discontinuity itself. Since the velocity jump at the 410 is around +4% in spherical Earth's models (Kennett and Engdahl, 1991), the corresponding first-order jump associated with these zones could be near $\Delta vs = -2$–4%. This value is a lower bound, as larger Δvs values would be required if a velocity gradient was extended over a larger depth interval.

The corner-frequency for our receiver function work is 0.2 Hz and the station spacing for F-Net is coarse compared with the 0.5 Hz corner-frequency and the dense Hi-Net array used by Kawakatsu and Yoshioka (2011). As a result, we do not clearly image a dipping low-velocity layer associated with the MOW in southwest Japan. We find, however, a broad zone of negative amplitudes from ∼420 to ∼500 km depth right below the deepest cluster of earthquakes near 135°W longitude (Figs. 2a and S2).

In Fig. 2b we plot a cross-section through the model of Debayle and Ricard (2012) along the A-a profile. The limited horizontal resolution of this global surface-wave model, derived from long-period data, means that the fast velocity anomalies associated with the Pacific plate in the upper mantle tend to spread. As a result the Philippine Sea plate remains indistinct between broad back-arc low-velocity anomalies. However, this global model shows distinctive fast velocity anomalies in the MTZ. By comparison, the body-wave tomographic models (Fig. S11) provide more specific locations for the Pacific and Philippine Sea plates in the upper mantle, and also reveal fast velocity material in the MTZ.

In Figs. 2c and S11b, d, f, we superimpose the results from the scattered waves on the tomographic images. To focus on the seismic signature of solid–solid phase transitions from low to high-pressure assemblages with increasing density and velocities, seismologists usually emphasize positive RF signals in the mantle. Here in contrast, we emphasize negative signals (black filled waveforms). Our purpose is to enhance the spatial correlation between the negative zones of reflectivity and the presence of the Pacific plate in the MTZ. In this case (Figs. 2c and S11b, d, f), the dipping portion of Z2 (in the frame) appears to delineate the bottom of the Pacific fast anomaly as seen in Debayle and Ricard (2012)'s model (Fig. 2), and other models shown in Fig. S11. Based on the geometry of subduction with the A-a profile crossing the Izu-Bonin subduction trench in the east (Fig. 1), we identify the fast body in

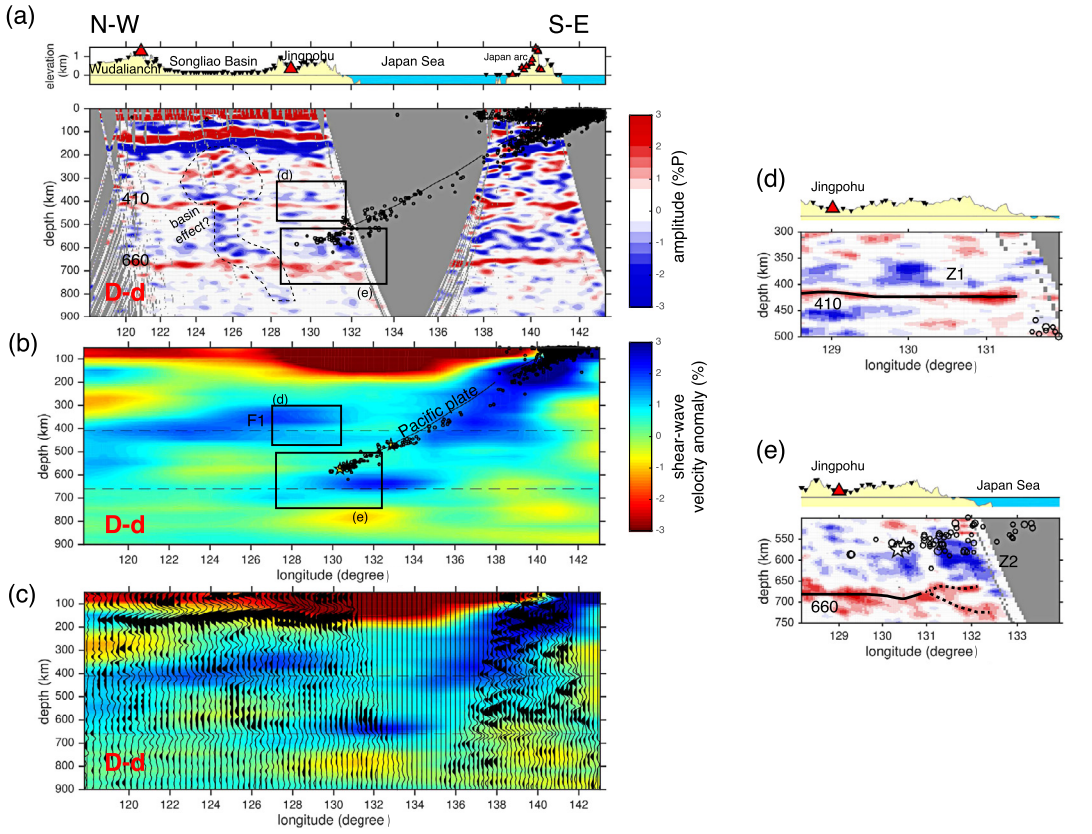

Fig. 5. (a) CCP section for the D-d profile. Positive/negative amplitudes are shown in red/blue and mark shear-wave velocity increase/decrease. The seismicity (black dots) is associated with the subduction of the Pacific plate from the Japan Trench. A complicated pattern of amplitudes (contoured with a dashed line) extends below the Songliao Basin from the shallow mantle down to the base of the transition zone. The two insets correspond to enlarged views of the results shown in panels (d) and (e). (b) Cross-section through the shear-wave velocity model of Debayle and Ricard (2012). (c) Superimposition of the CCP section on the tomographic model – negative amplitudes are emphasized in black. (d) A zoom around the 410-km discontinuity. (e) A zoom around the 660-km discontinuity. Earthquakes with magnitude larger than 7.0 are indicated with a star.

the lowermost MTZ between 136°W and 142°W (F2) as a deep portion of the Pacific plate subducting below the Philippine Sea plate (Fig. 2b). This small portion coincides with the isolated zone of reflectivity Z2 between 136°W and 140°W. The shallower zone, Z1 (in the frame in Fig. 2a), overlies the fast Pacific slab anomalies in the MTZ (Fig. 2c).

Although profile B-b has a different orientation (Fig. 1), it does not lie far from A-a, and therefore gives comparable images in term of reflectivity structure and tomography (cf. Figs. 2 and 3). In the west, profiles A-a and B-b use RF data from different networks (the F-Net array in Japan and the permanent network in Korea), and sample different shallow structures (the Philippine Sea plate in subduction along A-a compared with a simple continental crust in Korea along B-b). Consequently the similarity in the deep reflectivity structure, including both reflectivity zones, cannot result from instrumental or shallow structural effects such as reverberations. The reflectivity patterns in Z1 and Z2 are even more visible along this second profile. We note strong negative signals within and surrounding the MTZ between 130 and 134°E. Along the western portion of B-b (125°W–131°W in Fig. 3a), Z2 is a broad (100-km thick) and flat region of negative reflectivity. In the east however, the reflectivity zone (Fig. 3e) is more complex, and appears to delimit the fast velocity of the body labeled F2 below the Izu-Bonin arc (Fig. 3b). Z1 is located at the root of a broad region of negative velocity anomalies (L1) between 126°W and 131°W in the tomographic models (Figs. 3b and S12) or stuck in the east between the subducting portion of the Pacific plate in the upper mantle and the stagnant portion in the MTZ (Figs. 3b and S12). A significant depth variation of Z1 is found in this eastern zone with its upper boundary rising toward the east from around 390 km to near 330 km over about 150 km lateral distance (Fig. 3d).

3.2. *Long-range seismic profile from Japan to China through the Korean peninsula (C-c)*

Profile C-c (Fig. 4) confirms the general characteristics of the bands of reflectivity Z1 and Z2 seen in the previous figures. Z2 is ~100-km thick (Fig. 4e) and marks the base of the stagnant Pacific plate in the MTZ (Figs. 4b, c and S12). Z1 is located above the plate, but has a complex signature with a bi-modal depth distribution with peaks at 390 km and 350 km depths (Fig. 4a, d). This Z1 zone of reflectivity tends to shallow toward the East, and lies at the root of a broad region of low-velocity anomalies (L1) below the Chugaryung intra-plate volcano (Fig. 4b). It is unclear if the zone of blurred signals in the CCP image between 40°N and 44°N (dashed contour in Fig. 4a) is related to multiple reverberations in the southern part of the Songliao basin (Liu et al., 2015) or related to a sharp structural boundary near 42°N, as seen in the tomographic models (Figs. 4b and S12). This style of interference pattern is also observed along D-d (Fig. 5) and other profiles across northern China shown in the Supplementary Material (Figs. S9–S10). A coherent feature is the flat negative anomaly at ~600 km depth between 43 and 47°N north-northwest of the Songliao basin. We do not discuss the complex dipping arrivals at 30°N–34°N, that are probably related to the subduction of the

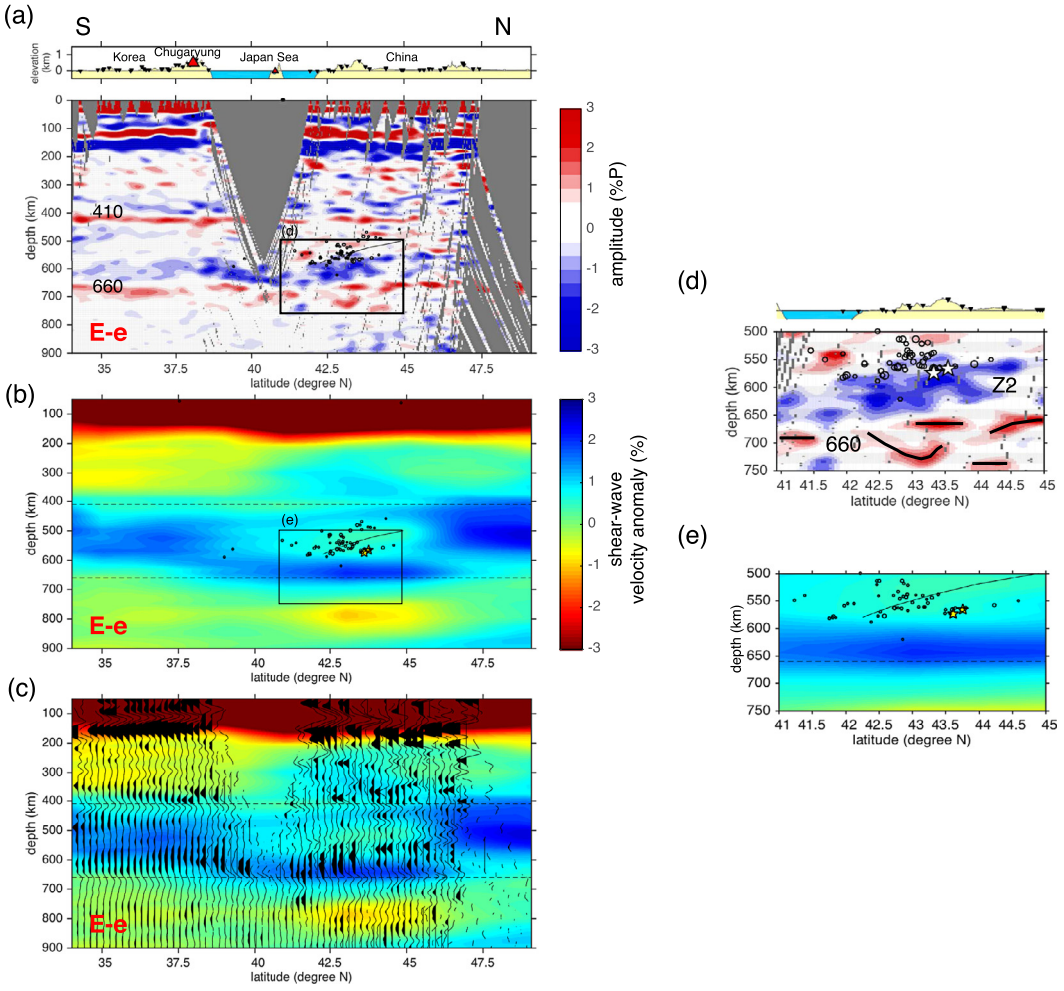

Fig. 6. (a) CCP section for the E-e profile. Positive/negative amplitudes are shown in red/blue and mark shear-wave velocity increase/decrease. The seismicity is shown with black dots. The insets correspond to zooms on the RF signal in panel (d) and tomography in (e). (b) Cross-section through the shear-wave velocity model of Debayle and Ricard (2012). (c) Superimposition of the CCP section on the tomographic model – negative amplitudes are emphasized in black. (d–e) Enlarged views on the RF signal and the tomographic model near the 660-km discontinuity and the deep cluster of seismicity. Earthquakes with magnitude larger than 7.0 are indicated with a star.

Philippine Sea plate and the occurrence of multiple reverberations on top of the plate.

3.3. Sampling the deep cluster of seismicity in the MTZ below the Japan Sea (D-d and E-e)

We also present CCP sections for two additional profiles (Figs. 5 and 6) that cross the clusters of deep seismicity in the transition zone at the East Asian margin below the Japan Sea (Fig. 1). The first profile (D-d) is perpendicular to the Japan Trench, and the second (E-e) samples the tip of the Wadati–Benioff zone of the Pacific plate in the transition zone (Hayes et al., 2012). In both sections, the deepest cluster of earthquakes overlies the Z2 reflectivity zone on top of the '660' km discontinuity (Figs. 5e and 6d). The Z2 zone of reflectivity is coincident with a portion of the subducted Pacific plate at the base of the MTZ with elevated S wavespeed in the model of Debayle and Ricard (2012) over the region between 37.5°–45°N latitude and 128°–135°W longitude (Figs. 5b and 6b, e). Z2 is also coincident with a zone of doubled (or at least complicated) 660 (Figs. 5e and 6d), as previously reported in the studies of Niu and Kawakatsu (1996), Ai et al. (2003) and Tian et al. (2016). In Fig. 5, the complex conversions at 136–142°E in the MTZ may correspond to a combination of Z2 and multiple reverberation occurring atop the Pacific subducted plate.

3.4. Geographical extent of the reflective zones

The maps in Figs. 7a and 8a show the geographical distribution of the negative reflectivity within the two depth windows of Z1 (325–400 km) and Z2 (560–660 km). The gray area corresponds to regions with no coverage by piercing points. Detection is positive when the average conversion amplitude in this depth interval exceeds one standard deviation from the bootstrap resampling (level at 68%) and is negative (blue). This means that 68% of the models obtained with the bootstrap analysis have amplitude less than zero at that location. White areas represent seismic amplitudes below the noise level, either because conversion amplitudes are weak, or the noise level is high (see Fig. S13).

In the 325–400 km depth range (Fig. 7a), we identify four major zones of positive detections of Z1, labeled from I to IV. The largest area is located below the Korean peninsula and Kyushu (I). The second (II) is located below the Songliao sedimentary basin in northeast China. The third and fourth zones are located below Hokkaido and Honshu (III and IV). Below Honshu (zone IV in Fig. 7b), the low-velocity zone almost coincides geographically with the Wadati–Benioff zone in the same depth range.

In the 560–660 km depth range for Z2 (Fig. 8a), we find three major zones of negative reflectivity. Zone I is more or less the same area as for Z1, except that it extends somewhat further west towards the Yellow Sea. The second zone is patchy and located below

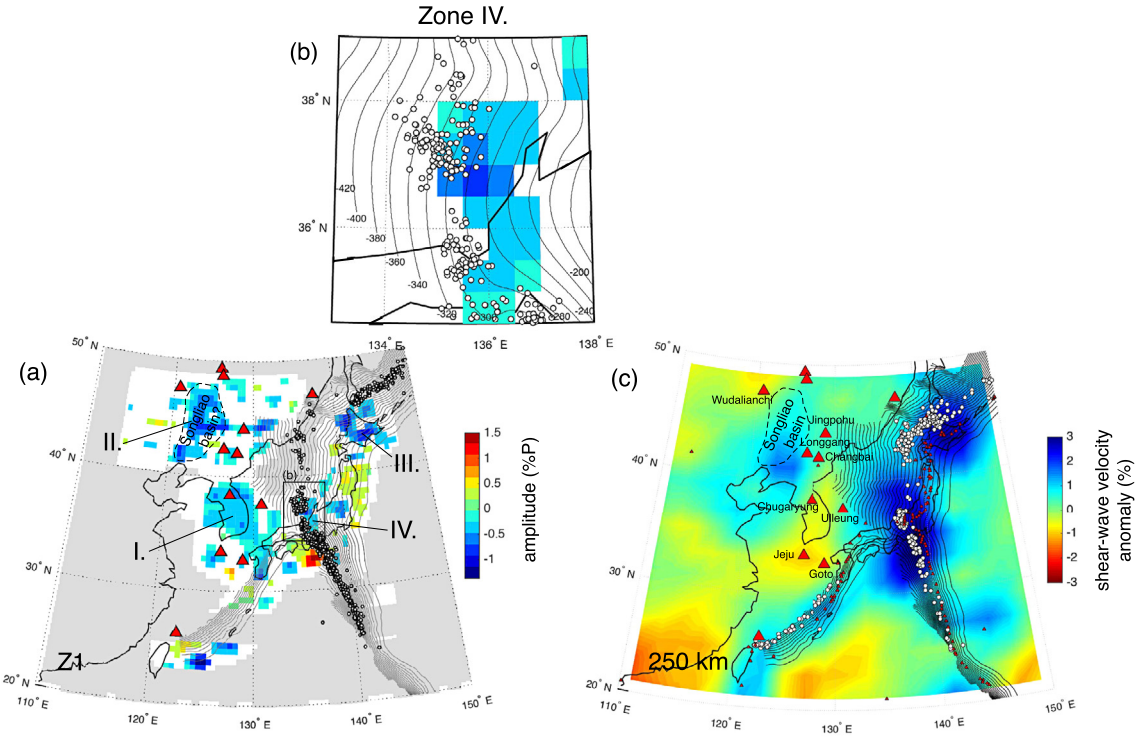

Fig. 7. (a) Map of the amplitude of seismic signals in the shallower zone of reflectivity Z1 (325–400 km depth range). Area in gray have no data coverage. The zone in white marks the region where CCP stacked amplitudes do not exceed the 68% confidence level. Zones in red and blue mark regions with dominantly positive or negative amplitudes, and exceeding the 68% confidence level. Z1 is therefore observed in four major zones in blue (labeled I, II, III and IV). The black frame in Japan locates the zone IV that is enlarged in (b). Deep subduction zone earthquakes within the same depth range are located with black circles. Red triangles indicate major intra-plate volcanic fields. (b) Comparison between Z1 and the seismicity in the same depth range. The depth corresponding to the slab contours is indicated. (c) Cross-section at 250 km depth in the shear-wave tomographic model of Debayle and Ricard (2012). The slab contours (black lines) and seismicity (white dots) are superimposed. Intra-plate volcanic fields are labeled and marked with red triangles.

the Songliao basin. Finally, the third zone shows the strongest amplitudes (−1% the P-wave amplitude) and is located at the tip of the deepest contours of the subducted Pacific plate in the model of Hayes et al. (2012). The pattern of low-velocity zones in this zone III locates strikingly near the clusters of earthquakes at depths greater than 550 km (Fig. 8b).

In Fig. 7a, c, Z1 in zone I is rooted below broad low-velocity anomalies in the upper-mantle in East Asia, below major intra-plate volcanic fields. Z2 in zones I and III is embedded in the fast seismic signature of stagnant portions of the Pacific plate in the MTZ (Fig. 8c, d). The Songliao basin (zone II in Figs. 7 and 8) is a singular place in the region, with Z1 at the root of a broad fast velocity anomaly in the upper-mantle and above a slow velocity anomaly in the MTZ (Figs. 7c and 8c).

4. Discussion

4.1. Summary of our observations

The presented reflectivity profiles clearly reveal the MTZ solid–solid phase changes beneath Eastern Asia and the Pacific Northwest. Importantly, our observations support previous observations of apparent low-velocity zones on top of the 410, within the MTZ (Revenaugh and Sipkin, 1994; Tauzin et al., 2010; Liu et al., 2015; Shen et al., 2008; Gao et al., 2010; Shen et al., 2014), and of seismic scattering in the same region (Bentham and Rost, 2014). The zones of reflectivity are pervasive and complex. They show apparent topography of about 60 km over 150 km lateral distance (Fig. 3d, e), can be broad (up to ∼100 km thick for Z2 in Figs. 4e, 5e, 6d), or present a bi-modal depth distribution such as Z1 in Fig. 4d or Z2 in Fig. 3e. Bentham and Rost (2014) showed in their P–P scattering study that scatterer locations are correlated with the edges of fast velocity features in the MTZ. With the exception of the region below the Songliao basin (Fig. S9–S10), the reflective zones in our study also delineate the high seismic wave speeds of the plates in the MTZ (e.g. Fig. 3c). Z2 is located at the base of the Pacific slab whereas Z1 is located on top of the plate (Figs. 7 and 8). We show here that the reflectivity in RF imaging has dominantly a negative signature, i.e. suggestive of a downward *vs* reduction.

4.2. Possible artifacts

Spurious signals in CCP sections derived from receiver functions can arise from various reasons, in some cases without any relation with the Earth's mantle structure. The most common origins are seismic noise on raw and deconvolved seismograms, sidelobes due to signal processing artifacts, in particular from deconvolution, interference of seismic phases, contamination by multiple reverberations within the uppermost mantle structure, or approximations in the physics underlying the imaging principle. We show in the supplementary material (Section S3) that major features discussed in section 3 are robust because their stacked amplitudes exceed the noise level (Figs. S13–S14). The negative arrivals associated with Z1 and Z2 cannot result from multiple reverberations because they have slowness similar to the conversions at the 410-km and 660-km discontinuities (Fig. S15). One of the physical assumptions underlying our imaging principle is the use of a one-dimensional Earth's model for ray-tracing and back projection. We show in Fig. S16 that using a three-dimensional model does not change much the overall pattern of stacked amplitudes. Potential problems may arise in our imaging from projecting the 3D structure

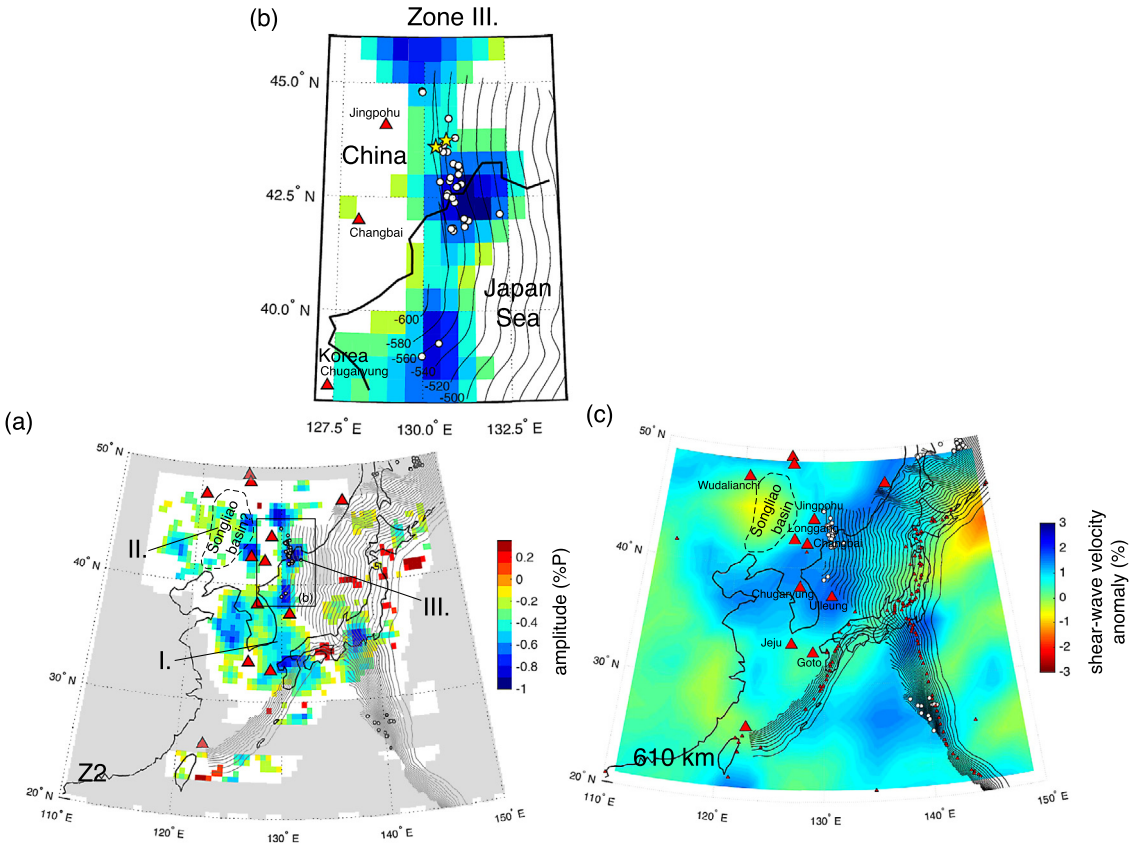

Fig. 8. (a) Map of the amplitude of seismic signals in the deeper zone of reflectivity Z2 (560–660 km depth range). Deep subduction zone earthquakes are located with black dots, intra-plate volcanic fields with red triangles, and the frame marks the region enlarged in (b). We identify three major zones, labeled I, II and III. (b) Enlargement of zone III, emphasizing the local coincidence between Z2 and the seismicity in the same depth range. Earthquakes with magnitude larger than 7.0 are plotted with yellow stars. The depth corresponding to the slab contours is indicated. (c) Cross-section at 610 km depth in the shear-wave tomographic model of Debayle and Ricard (2012). The slab contours (black lines) and seismicity (white dots) are superimposed. Intra-plate volcanic fields are labeled and marked with red triangles.

at large distances onto 2D profiles. We tested (Section S3 in the supplementary material) the effect of CCP stacking using profiles along different directions, with rectangular bins of different sizes, or using circular bins. We mainly found an effect on the signal-to-noise ratio of the image (smaller bins give less data to stack, and a higher noise level), but not really on the recovered structure itself, suggesting a limited bias introduced by projection. The effect of not accounting for the effect of physical scattering, i.e. the deviation of rays by heterogeneities in the medium properties, is more difficult to judge but we believe that many contiguous diffraction points would be required to explain our results across such a large scale. Finally, we show in Figs. S4–S8 that sidelobe and phase interference effects are too faint (one third of the amplitude observed on the data) to fully explain the observed negative reflectivity at the base of the transition zone.

4.3. Analogy with the Pacific Northwest (western US)

A similar type of seismic signature to that seen in the northwest Pacific has been found in the MTZ below western US (Song et al., 2004; Tauzin et al., 2013; Hier-Majumder and Tauzin, 2017). Fig. 9 presents the result of CCP stacking of receiver functions along a profile (F-f) extending from the Sierra Nevada in the southwest to the cratonic province northeast of the Rocky Mountains (Fig. 9a, b). In teleseismic body-wave travel-time tomography (e.g. Burdick et al., 2010), the craton is observed in the northeast as a fast velocity anomaly (F1) extending down to the base of the upper mantle (Fig. 9c). The profile F-f crosses the large domain of extensional tectonics in the Basin and Range province, and also the time-progressive sequences of silicic centers in the Yellowstone-Snake River Plain region. Slow-velocity anomalies are pervasive in the upper mantle below these extensional and volcanic regions, which lie above a large fast-velocity body stalled within the MTZ. This seismically fast material has been attributed to a remnant of the former Farallon plate. Fig. 9b shows two negative signals, on top of the 410 and a weaker feature near 590 km depth, delimiting the fragment of the Farallon plate in the MTZ. Along profile F-f, Z1 has its strongest signature below the western Snake River plain (Hier-Majumder and Tauzin, 2017). Z2 has been shown to be spatially coincident with the fast velocity anomalies in the MTZ (Tauzin et al., 2013).

4.4. On the origin of the negative seismic reflectivity/scattering zones

Z2 could be consistent in polarity with a negative velocity gradient associated with the base of the cold thermal plates in the MTZ. However, we partly reject this hypothesis. At 500 km depth, for an approximate thermal model corresponding to subduction in North Honshu (see Section S4 in supplementary material), we estimate that the temperature would drop from ~1730 K, the temperature given by the 1600 K adiabatic gradient, to ~750 K in the coldest part of the slab (Fig. 10a). This ~1000 K gradient would occur over approximately 150 km vertical distance (Fig. 10a), and therefore be of ~6.7 $K\,km^{-1}$. Given the partial derivatives of shear-wave velocity with respect to temperature for a pyrolite-like mantle composition ($K = -7.0 \times 10^{-5}\ K^{-1}$; Stixrude and Lithgow-Bertelloni, 2005), and without accounting for mineralogical phase transitions, the expected reduction in shear-wave velocity over this vertical distance would be of ~0.3 $km\,s^{-1}$, i.e. ~7%. This amplitude of velocity jump is equiva-

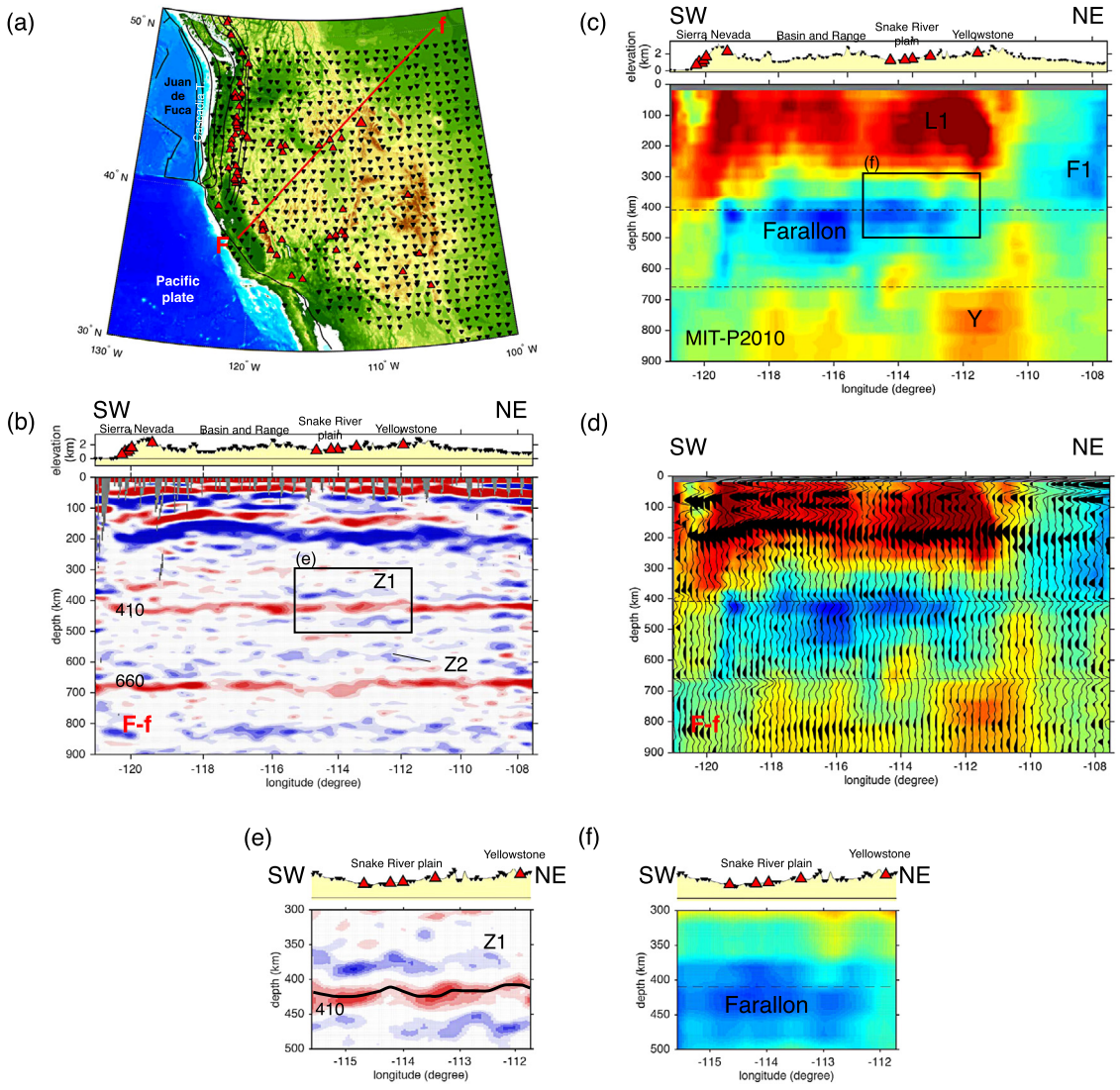

Fig. 9. (a) Map of the western US with stations (black triangles), Quaternary active volcanoes (red triangles), with the location of the F-f profile. 820 broad-band stations from the Transportable Array are used for the receiver function analysis (Tauzin et al., 2013). The depth contours of the subducted Juan de Fuca plate are shown with black lines from 20 km to 100 km depths. Red triangles indicate Quaternary active volcanoes. (b) CCP section along the F-f profile. Positive/negative amplitudes are shown in red/blue and mark shear-wave velocity increase/decrease. The inset corresponds to enlarged view on the RF signal in panel (e) and tomography in (f). (c) Cross-section through the P-wave tomographic model MIT-P2010 of Burdick et al. (2010). Major interpreted features are: F1, a fast velocity anomaly associated with the cratonic province in the western US. L1: a large low-shear wave velocity anomaly in the upper mantle below the Yellowstone and Snake River plain. Y: a low-velocity anomaly in the uppermost lower mantle possibly associated with the Yellowstone mantle plume. (d) Superimposition of the CCP section on the tomographic model. Negative amplitudes are emphasized in black. (e) Zoom on the RF signal near the 410-km discontinuity below the Yellowstone and Snake River plain. (f) Tomographic velocity anomalies within the same frame as (e). The color scales saturate at ±2.5% of the P-wave amplitude for RF sections and ±1.2% for tomographic velocity anomalies.

lent to the vs jump at the 660-km discontinuity (Fig. 10b). We have made a synthetic test for the recovery of such a thermal gradient from RF imaging. The result is shown in Fig. 10e. The RF signal has its strongest amplitude at places where the vs gradient is the steepest, and we find that it is not possible to fully recover broad velocity gradients over ∼150 km depth. In addition, the amplitude of recovery of the gradient in its steepest part is of the same order as the amplitude of sidelobes for the *iasp91* structure (Fig. 10d). Using a partial derivative K at the higher bound of the values estimated for minerals in the MTZ ($K = -12.0 \times 10^{-5}$ K^{-1}; Stixrude and Lithgow-Bertelloni, 2005) allows a better recovery of the gradient but still underestimates seismic amplitudes by a factor 2 to 3 (Figs. 10c and 10f). In conclusion, it is difficult to explain the strong negative signal at the base of the transition zone Z2 with a simple thermal gradient at the base of the plate alone.

Concerning zone Z1, the prominent negative phases in the CCP stacks – indicative of a velocity drop with increasing depth – are found exactly on top of fast velocity structures in tomographic images. The background velocity gradient arising from such fast structures should be positive, not negative. We do not find systematic fast velocity anomalies in the upper mantle that may explain a velocity drop in Z1 (Fig. 7). Therefore we reject the idea that Z1 marks the base of cold slabs in the upper mantle. The potential presence of a low-velocity zone (Z1) on top of fast (and cold) velocity structures in tomographic images (Figs. 2–6 and 9) is a main reason for invoking the effect of compositional heterogeneities, in particular volatile elements (e.g. Hier-Majumder and Tauzin, 2017), on mantle rock properties.

4.5. General implications and some speculations

Our observations could be important for the general understanding of the global dynamics of mantle convection and the recycling of geochemical heterogeneities. The cold signature of

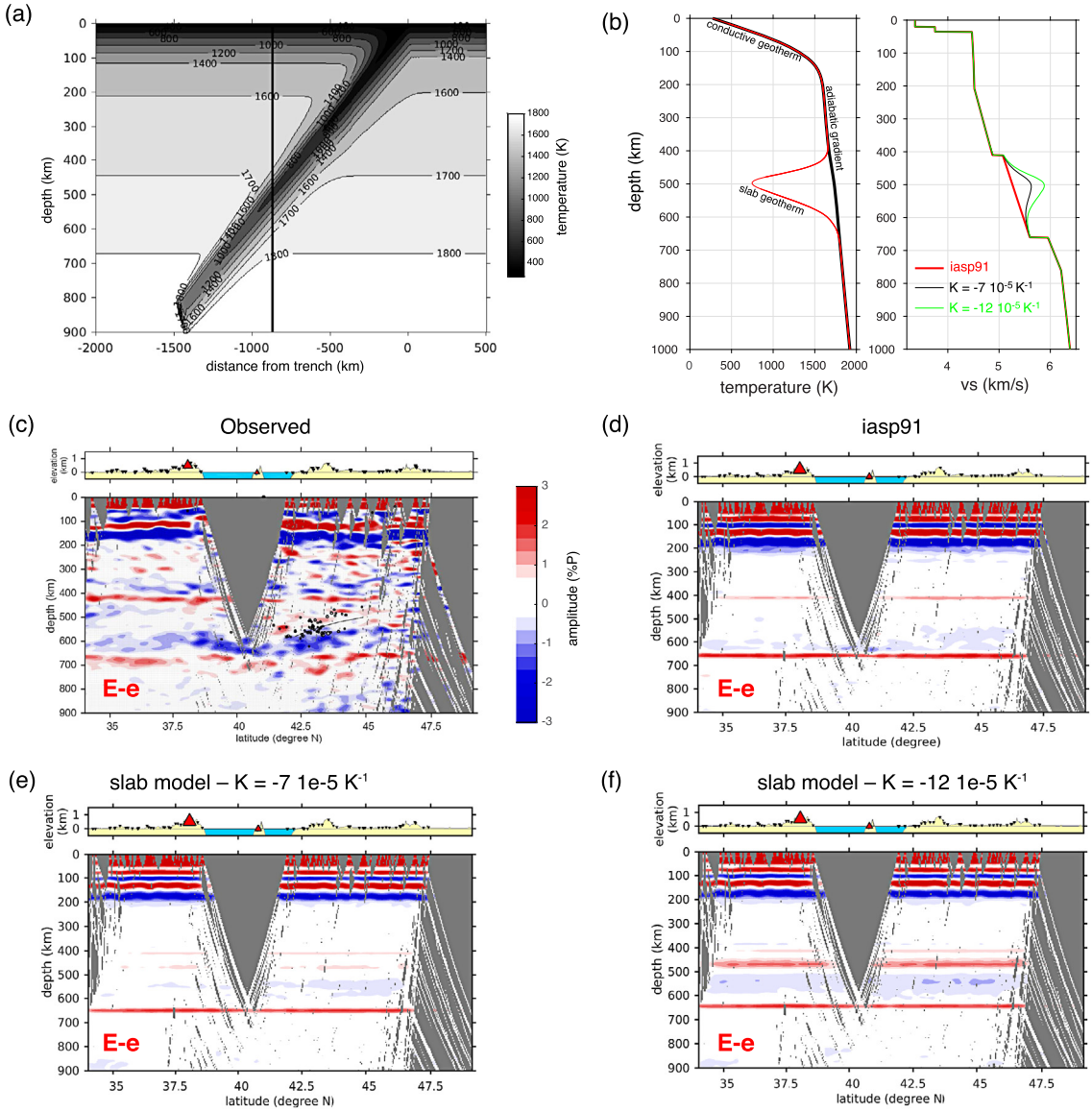

Fig. 10. (a) Simplified thermal model with parameters consistent with plate subduction at the trench in North Honshu (see Section S4 of supplementary material for the set-up of this model). The vertical black line at ~ -870 km distance from the trench corresponds to the temperature and shear-wave velocity profiles shown in (b). (b) Conductive, adiabatic and slab geotherms (left), and the shear-wave velocity profiles obtained from perturbing the iasp91 velocity model (Kennett and Engdahl, 1991) using different partial derivatives of *vs* with respect to temperature, $K = -7.0 \times 10^{-5}$ K^{-1} (Stixrude and Lithgow-Bertelloni, 2005) and $K = -12.0 \times 10^{-5}$ K^{-1}. (c) Observed seismic section along the E-e profile. (d) Synthetic section along the same profile using the *iasp91* velocity structure. (e) Synthetic section for the perturbed *iasp91* velocity model and $K = -7.0 \times 10^{-5}$ K^{-1}. (f) Synthetic section for $K = -12.0 \times 10^{-5}$ K^{-1}.

subducted plates dominates in the long-wavelength tomographic images of the East Asia margin. In contrast as shown by our simple synthetic test in Fig. 10, receiver functions may reveal complexity at smaller scale that could be the result of compositional heterogeneity. There are indications of a global distribution of these zones on top of the $ol \rightarrow wa$ and $rw \rightarrow pv + mw$ phase transitions (Vinnik and Farra, 2007; Tauzin et al., 2010; Shen et al., 2014). Several end-member geodynamical models have been proposed to explain a potential chemical stratification in the MTZ. Two of them involve filtering of the major (Fe, Mg, Al, Si) and minor (H, C) element chemistry by MTZ solid–solid phase changes (Ringwood and Irifune, 1988; Bercovici and Karato, 2003).

Convective mass transfer across the boundaries of the MTZ can cause dehydration melting if the water content in the MTZ exceeds the smaller water storage capacity of the shallower *ol* and deeper $pv + mw$ mantle minerals (Bercovici and Karato, 2003; Richard and Bercovici, 2009). This process of chemical filtering on top of the 410-km discontinuity could explain the difference in composition of mid-oceanic ridge and oceanic island basalts (Bercovici and Karato, 2003). Many observations of negative zones have been attributed to this process (see Tauzin et al., 2010 and references therein), including recent ones at the top of the lower mantle below western US and northeast Asia (Schmandt et al., 2014; Liu et al., 2016). The zone atop the 660 (Z2) is not however a prediction from such a model.

The low-velocity zone near the base of the MTZ could provide compelling evidence for a change in bulk chemistry near the 660-km boundary. Chemical buoyancy relationships between the different constituents of subducted plates, MORB, hazburgite and pyrolite are expected to result in the trapping of compositional anomalies in a gravitationally stable layer between 600 and 700 km depths (Ringwood and Irifune, 1988; Nakagawa et al., 2010). This layer could be composed of oceanic crustal material (Van Keken et al., 1996; Nakagawa et al., 2010), or of a mixture of harzburgite and basalt (Ringwood and Irifune, 1988), with low-velocity signature (Shen and Blum, 2003). By impeding

mass transfers across the MTZ, this layer could affect the global pattern of mantle convection. Numerical models of slab sinking in the mantle (e.g. Ballmer et al., 2015) indeed suggest that a compositional stratification could explain the different observed regimes of slab subduction: slab deformation near the 660 then penetration into the lower mantle, penetration into the lower mantle with slab flattening at depths between 800 and 1050 km, and slab stagnation into the MTZ (Fukao and Obayashi, 2013).

Zhao (2004) and Richard and Iwamori (2010) suggested that the Cenozoic volcanism in East Asia, including in the Changbai volcanic area, could be explained through decompression melting assisted by hydrous upwelling originating from convective dehydration of the stagnant Pacific plate in the MTZ. The finding of an apparent LVZ on top of the 410-km discontinuity (Fig. 7) could reinforce their conclusion. Alternatively, the thermal destabilization of a compositionally distinct layer at the base of the MTZ could also act as a possible origin for deep buoyant plumes (Ringwood and Irifune, 1988). A mantle plume was proposed in the region of the Songliao basin and surrounding major intraplate volcanoes based on seismic tomography and receiver function observations (Tang et al., 2014; Liu et al., 2015).

It is also reasonable to wonder if there is a link between Z2 and the presence of deep focus earthquakes (>550 km depth) in the MTZ, as the strongest Z2 appears in places where there is a concentration of these earthquakes (Fig. 8b). A common interpretation for the origin of these earthquakes is olivine metastability. Z2 below the Japan Sea can locally be associated with the 450–570 km deep MOW (Iidaka and Suetsugu, 1992; Kawakatsu and Yoshioka, 2011). Some authors however rather favor the effect of H_2O with dehydration embrittlement as a triggering mechanism. Alternatively, because the slab would meet resistance above the 600–700 km depth range, the high rate of deformation under relatively low temperatures could provide a favorable environment for shear instability and thermal runaway. The variations in material properties in the source region of deep subduction zone earthquakes, such as evidenced here, may also contribute to the diverse observed rupture behaviors (Ye et al., 2016).

The nature and underlying physical processes at the origin of these pervasive LVZs are debated and clearly not understood. In addition to the transitions in the olivine mineral and their kinetics, the non-olivine components (pyroxenes, garnet) increase the complexity of velocity gradients through additional solid–solid phase changes (e.g. Vacher et al., 1998). A possible illustration of this phenomenon is given in Figs. 5e and 6d where the 660 exhibits significant spatial complexity. This complexity has been attributed to multiple phase changes in the garnet component, from garnet-to-ilmenite and ilmenite-to-perovskite (Ai et al., 2003). Simmons and Gurrola (2000), Tauzin et al. (2013) and Cottaar and Deuss (2016) suggested the possible occurrence of such phase changes in the coldest regions of western US and Europe, too. A close examination of the spatial complexity of the MTZ may provide a clue on the chemical and thermal conditions driving to the formation of these deep zones of seismic scattering.

5. Conclusion

From receiver function imaging of the MTZ in the Northwestern Pacific and East Asia regions, we find two bands of pervasive seismic reflectivity with ∼50 km and ∼100 km thickness and apparent wave-speed reduction of −2% just above and at the base of the transition zone. These zones are geographically correlated with the stalled portions of the Pacific plate in the mantle transition zone. Similar features exist in the MTZ below western US in association with the Farallon plate. We speculate that the apparent LVZs are the signature of compositional heterogeneities, as revealed by numerous other studies of seismic scattering throughout the mantle, and that they could be widespread across the globe.

Acknowledgements

We thank the IRIS Data Management Center, the Korea Institute of Geosciences and Mineral Resources, the Korean Meteorological Administration, and the NIED F-net providing the waveform data used in this study. B.T. was funded with a Délégation CNRS and Congé pour Recherches et Conversion Thématique from the Université de Lyon at the Research School of Earth Sciences (RSES), Australian National University (ANU). We thank the CNRS, Université de Lyon, and ANU, for providing the funding and research environment. S.K. was funded by the Korean Meteorological Administration Research and Development Program under grant KMIPA2017-4020. We thank Julian Byrne for providing support for calculations on the ANU Terrawulf cluster, a computational facility developed with support from the AuScope initiative. AuScope Ltd is funded under the National Collaborative Research Infrastructure Strategy (NCRIS), an Australian Commonwealth Government Programme. We thank Juan-Carlos Afonso for helping in adjusting the parameters for the slab thermal model. We thank A.M. Negredo for making available TEMSPOL. We thank Luciana Bonatto for a constructive discussion during the EGU meeting 2017. We thank Yanick Ricard, Hrovje Tkalčić, Eric Debayle and Jean-Philippe Perrillat for constructive suggestions that helped to improve early versions of this manuscript.

Appendix A. Supplementary material

Supplementary material related to this article can be found online at http://dx.doi.org/10.1016/j.epsl.2017.08.006.

References

Ai, Y., Zheng, T., Xu, W., He, Y., Dong, D., 2003. A complex 660 km discontinuity beneath northeast China. Earth Planet. Sci. Lett. 212 (1), 63–71.

Ballmer, M.D., Schmerr, N.C., Nakagawa, T., Ritsema, J., 2015. Compositional mantle layering revealed by slab stagnation at ∼1000-km depth. Sci. Adv. 1 (11), e1500815.

Bentham, H.L.M., Rost, S., 2014. Scattering beneath Western Pacific subduction zones: evidence for oceanic crust in the mid-mantle. Geophys. J. Int. 197 (3), 1627–1641.

Bercovici, D., Karato, S.I., 2003. Whole-mantle convection and the transition-zone water filter. Nature 425 (6953), 39–44.

Bina, C.R., Helffrich, G., 1994. Phase transition Clapeyron slopes and transition zone seismic discontinuity topography. J. Geophys. Res., Solid Earth 99 (B8), 15853–15860.

Burdick, S., van der Hilst, R.D., Vernon, F.L., Martynov, V., Cox, T., Eakins, J., Pavlis, G.L., 2010. Model update January 2010: upper mantle heterogeneity beneath North America from traveltime tomography with global and USArray transportable array data. Seismol. Res. Lett. 81 (5), 689–693.

Cottaar, S., Deuss, A., 2016. Large-scale mantle discontinuity topography beneath Europe: signature of akimotoite in subducting slabs. J. Geophys. Res., Solid Earth 121 (1), 279–292.

Courtier, A.M., Revenaugh, J., 2007. Deep upper-mantle melting beneath the Tasman and Coral Seas detected with multiple ScS reverberations. Earth Planet. Sci. Lett. 259 (1), 66–76.

Debayle, E., Ricard, Y., 2012. A global shear velocity model of the upper mantle from fundamental and higher Rayleigh mode measurements. J. Geophys. Res., Solid Earth 117 (B10).

Efron, B., Tibshirani, R., 1990. Statistical Data Analysis in the Computer Age. University of Toronto, Department of Statistics.

Fukao, Y., Obayashi, M., 2013. Subducted slabs stagnant above, penetrating through, and trapped below the 660 km discontinuity. J. Geophys. Res., Solid Earth 118 (11), 5920–5938.

Gao, Y., Suetsugu, D., Fukao, Y., Obayashi, M., Shi, Y., Liu, R., 2010. Seismic discontinuities in the mantle transition zone and at the top of the lower mantle beneath eastern China and Korea: influence of the stagnant Pacific slab. Phys. Earth Planet. Inter. 183 (1), 288–295.

Green, H.W., Houston, H., 1995. The mechanics of deep earthquakes. Annu. Rev. Earth Planet. Sci. 23 (1), 169–213.

Hayes, G.P., Wald, D.J., Johnson, R.L., 2012. Slab1.0: a three-dimensional model of global subduction zone geometries. J. Geophys. Res., Solid Earth 117 (B1).
Hier-Majumder, S., Tauzin, B., 2017. Pervasive upper mantle melting beneath the western US. Earth Planet. Sci. Lett. 463, 25–35.
Iidaka, T., Suetsugu, D., 1992. Seismological evidence for metastable olivine inside a subducting slab. Nature 356 (6370), 593.
Kaneshima, S., 2016. Seismic scatterers in the mid-lower mantle. Phys. Earth Planet. Inter. 257, 105–114.
Kawakatsu, H., Yoshioka, S., 2011. Metastable olivine wedge and deep dry cold slab beneath southwest Japan. Earth Planet. Sci. Lett. 303 (1), 1–10.
Kennett, B.L.N., Engdahl, E.R., 1991. Traveltimes for global earthquake location and phase identification. Geophys. J. Int. 105 (2), 429–465.
Kim, S., Tkalčić, H., Rhie, J., Chen, Y., 2016. Intraplate volcanism controlled by back-arc and continental structures in NE Asia inferred from transdimensional Bayesian ambient noise tomography. Geophys. Res. Lett. 43 (16), 8390–8398. http://dx.doi.org/10.1002/2016GL069483.
Kohlstedt, D.L., Keppler, H., Rubie, D.C., 1996. Solubility of water in the α, β and γ phases of $(Mg,Fe)_2SiO_4$. Contrib. Mineral. Petrol. 123 (4), 345–357.
Ligorría, J.P., Ammon, C.J., 1999. Iterative deconvolution and receiver-function estimation. Bull. Seismol. Soc. Am. 89 (5), 1395–1400.
Liu, Z., Park, J., Karato, S.I., 2016. Seismological detection of low velocity anomalies surrounding the mantle transition zone in Japan subduction zone. Geophys. Res. Lett. 43, 2480–2487.
Liu, Z., Niu, F., Chen, Y.J., Grand, S., Kawakatsu, H., Ning, J., Ni, J., 2015. Receiver function images of the mantle transition zone beneath NE China: new constraints on intraplate volcanism, deep subduction and their potential link. Earth Planet. Sci. Lett. 412, 101–111.
Nakagawa, T., Tackley, P.J., Deschamps, F., Connolly, J.A., 2010. The influence of MORB and harzburgite composition on thermo-chemical mantle convection in a 3-D spherical shell with self-consistently calculated mineral physics. Earth Planet. Sci. Lett. 296 (3), 403–412.
Niu, F., 2014. Distinct compositional thin layers at mid-mantle depths beneath northeast China revealed by the USArray. Earth Planet. Sci. Lett. 402, 305–312.
Niu, F., Kawakatsu, H., 1996. Complex structure of mantle discontinuities at the tip of the subducting slab beneath northeast China. J. Phys. Earth 44 (6), 701–711.
Ohtani, E., Toma, M., Litasov, K., Kubo, T., Suzuki, A., 2001. Stability of dense hydrous magnesium silicate phases and water storage capacity in the transition zone and lower mantle. Phys. Earth Planet. Inter. 124 (1), 105–117.
Revenaugh, J., Sipkin, S.A., 1994. Melt atop the 410-km mantle discontinuity. Nature 369, 9.
Ricard, Y., Mattern, E., Matas, J., 2005. Synthetic tomographic images of slabs from mineral physics. In: Earth's Deep Mantle: Structure, Composition, and Evolution, pp. 283–300.
Richard, G.C., Iwamori, H., 2010. Stagnant slab, wet plumes and Cenozoic volcanism in East Asia. Phys. Earth Planet. Inter. 183 (1), 280–287.
Richard, G.C., Bercovici, D., 2009. Water-induced convection in the Earth's mantle transition zone. J. Geophys. Res., Solid Earth 114 (B1).
Ringwood, A.E., Irifune, T., 1988. Nature of the 650-km seismic discontinuity: implications for mantle dynamics and differentiation. Nature 331, 131–136.
Schmandt, B., Jacobsen, S.D., Becker, T.W., Liu, Z., Dueker, K.G., 2014. Dehydration melting at the top of the lower mantle. Science 344 (6189), 1265–1268.
Shen, X., Yuan, X., Li, X., 2014. A ubiquitous low-velocity layer at the base of the mantle transition zone. Geophys. Res. Lett. 41 (3), 836–842.
Shen, X., Zhou, H., Kawakatsu, H., 2008. Mapping the upper mantle discontinuities beneath China with teleseismic receiver functions. Earth Planets Space 60 (7), 713–719.
Shen, Y., Blum, J., 2003. Seismic evidence for accumulated oceanic crust above the 660-km discontinuity beneath southern Africa. Geophys. Res. Lett. 30 (18).
Simmons, N.A., Gurrola, H., 2000. Multiple seismic discontinuities near the base of the transition zone in the Earth's mantle. Nature 405 (6786), 559–562.
Song, T.R.A., Helmberger, D.V., Grand, S.P., 2004. Low-velocity zone atop the 410-km seismic discontinuity in the northwestern United States. Nature 427 (6974), 530–533.
Stixrude, L., Lithgow-Bertelloni, C., 2005. Thermodynamics of mantle minerals—I. Physical properties. Geophys. J. Int. 162 (2), 610–632.
Tang, Y., Obayashi, M., Niu, F., Grand, S.P., Chen, Y.J., Kawakatsu, H., Ni, J.F., 2014. Changbaishan volcanism in northeast China linked to subduction-induced mantle upwelling. Nat. Geosci. 7 (6), 470–475.
Tauzin, B., Van Der Hilst, R.D., Wittlinger, G., Ricard, Y., 2013. Multiple transition zone seismic discontinuities and low velocity layers below western United States. J. Geophys. Res., Solid Earth 118 (5), 2307–2322.
Tauzin, B., Debayle, E., Wittlinger, G., 2010. Seismic evidence for a global low-velocity layer within the Earth's upper mantle. Nat. Geosci. 3 (10), 718–721.
Tian, Y., Zhu, H., Zhao, D., Liu, C., Feng, X., Liu, T., Ma, J., 2016. Mantle transition zone structure beneath the Changbai volcano: insight into deep slab dehydration and hot upwelling near the 410 km discontinuity. J. Geophys. Res., Solid Earth 121 (8), 5794–5808.
Vacher, P., Mocquet, A., Sotin, C., 1998. Computation of seismic profiles from mineral physics: the importance of the non-olivine components for explaining the 660 km depth discontinuity. Phys. Earth Planet. Inter. 106 (3), 275–298.
Van Keken, P.E., Karato, S., Yuen, D.A., 1996. Rheological control of oceanic crust separation in the transition zone. Geophys. Res. Lett. 23 (14), 1821–1824.
Vinnik, L., Farra, V., 2007. Low S velocity atop the 410-km discontinuity and mantle plumes. Earth Planet. Sci. Lett. 262 (3), 398–412.
Ye, L., Lay, T., Kanamori, H., Zhan, Z., Duputel, Z., 2016. Diverse rupture processes in the 2015 Peru deep earthquake doublet. Sci. Adv. 2 (6), e1600581.
Zhao, D., 2004. Global tomographic images of mantle plumes and subducting slabs: insight into deep Earth dynamics. Phys. Earth Planet. Inter. 146 (1), 3–34.